ELSEVIER

Computational and Theoretical Polymer Science 11 (2001) 329–343

Computational and Theoretical Polymer Science

www.elsevier.com/locate/ctps

Strategies for multiscale modeling and simulation of organic materials: polymers and biopolymers

William A. Goddard III*, Tahir Cagin, Mario Blanco, Nagarajan Vaidehi, Siddharth Dasgupta, Wely Floriano, Michael Belmares, Jeremy Kua, Georgios Zamanakos, Seichi Kashihara, Mihail Iotov, Guanghua Gao

Division of Chemistry and Chemical Engineering, California Institute of Technology, Materials and Process Simulation Center, 139-74, Pasadena, CA 91125, USA

Received 21 September 2000; revised 7 February 2001; accepted 9 February 2001

Abstract

Advances in theory and methods are making it practical to consider fully first principles (de novo) predictions of structures, properties and processes for organic materials. However, despite the progress there remains an enormous challenge in bridging the vast range of distances and time scales between de novo atomistic simulations and the quantitative continuum models for the macroscopic systems essential in industrial design and operations. Recent advances relevant to such developments include: quantum chemistry including continuum solvation and force field embedding, de novo force fields to describe phase transitions, molecular dynamics (MD) including continuum solvent, non equilibrium MD for rheology and thermal conductivity and mesoscale simulations. To provide some flavor for the opportunities we will illustrate some of the progress and challenges by summarizing some recent developments in methods and their applications to polymers and biopolymers. Four different topics will be covered: (1) hierarchical modeling approach applied to modeling olfactory receptors, (2) stabilization of leucine zipper coils by introduction of trifluoroleucine, (3) modeling response of polymers sensors for electronic nose, and (4) diffusion of gases in amorphous polymers.

Keywords: Quantum mechanics; Force field; Molecular dynamics

1. Introduction

In order to develop new materials and composites with designed new properties, it is essential that these properties be predicted before preparation, processing, and experimental characterization. Despite the tremendous advances made in the modeling of the structural, thermal, mechanical and transport properties of materials at the macroscopic level (finite element analysis of complicated structures) there remains tremendous uncertainty about how to predict many critical properties related to performance. The fundamental problem here is that these properties depend on the atomic level interactions and chemistry (e.g. making and breaking of bonds) dealing with the electronic and atomic level description at the level of nanometers and picoseconds. The materials designer needs answers from macroscopic modeling (finite element paradigm) of components having scales of centimeters and milliseconds or larger. To dramatically advance the ability to design useful high performance materials, it is essential that we insert the chemistry into the mesoscopic and macroscopic (finite element) modeling.

The difficulties in doing this are shown in Fig. 1, where we see that vast length and time scales separate the quantum mechanics (QM) from the macroscopic world of engineering design. Tremendous advances have been made recently in first principles QM predictions of chemical reactions, but the state of the art can handle accurately reactions with only ~50 atoms. There is no practical approach to carrying out a QM calculation on the initiation and propagation of a crack through a stabilized zirconia ceramic. Despite this difficulty, *the computations MUST be based on accurate first-principles QM if we are to predict the properties of new materials.*

Our *strategy* for accomplishing this objective is to develop an overlapping array of successively coarser modeling techniques. At each plateau (a range of length and time scales), the parameters of the coarse description are based on the parameters of the immediately finer description, as shown in Fig. 1. Thus based on accurate QM calculations we find a force field (FF) including charges, force constants, polarization, van der Waals

* Corresponding author. Tel.: +1-626-395-2731; fax: +1-626-585-0918.
E-mail address: wag@wag.caltech.edu (W.A. Goddard III).

1089-3156/01/$ - see front matter
PII: S1089-3156(01)00025-3

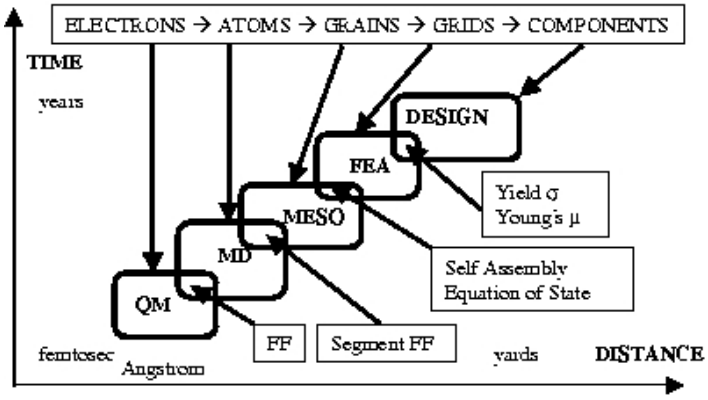

Fig. 1. Multiscale modeling hierarchy.

interactions etc that accurately reproduces the QM. With the FF, the dynamics is described with Newton's equations [molecular dynamics (MD)], instead of the Schrodinger Equation.

The MD level allows one to predict the structures and properties for systems $\sim 10^5$ times larger than for QM, allowing direct simulations for the properties of many interesting systems. This leads to many results relevant and useful in materials design, however, many critical problems in materials design require time and length scales far too large for practical MD.

Thus we need to develop methods treating the mesoscale in between the atomic length and time scales of MD and the macroscopic length and time scales (microns to mm and μs to s) of finite element analysis (FEA). This linking through the mesoscale in which we can describe microstructure is probably the greatest challenge to developing reliable first principles methods for practical materials' design applications.

Only by establishing this connection from microscale to mesoscale it is possible to build first principles methods for describing the properties of new materials and composites. Our aim is to reach the domain of materials science and engineering by building from fundamental principles of physics and chemistry. Thus, for fundamental predictions to play a direct role in materials innovation and design, it is essential to bridge the micro–meso gap. The problem here is that the methods of coarsening the description from atomistic to mesoscale or mesoscale to continuum is not so obvious as it was in going from electrons to atoms. For example, the strategy for polymers seems quite different than for metals, which seem different from ceramics or semiconductors.

Given the concepts, it is necessary to carry out calculations for realistic time scales fast enough to be useful in design. This requires developing software tools useful by design engineers, by incorporating the methods and results of the QM to MD to mesoscale simulations. To accomplish the goals of developing methods for accurate calculations of materials and properties, we focus on: (i) implementations that make full use of modern highly parallel computers, and (ii) building in knowledge based heuristic methods of accessing this information automatically so that designers can focus on the macroscopic issues without concern for the details of theory and simulation. At this point, we expect a revolution in materials design and innovations where the first-principles multiscale modeling and simulations play increasing role in the design stage and complementing the experiments.

2. Progress in methods developments

Our strategy is to transcend from the most fundamental theory (QM) to practical engineering designs in a sequence of several levels as indicated in Fig. 1.

2.1. Quantum mechanics

2.1.1. Ab initio quantum chemistry applications

It is important to use QM to describe systems in which bonds are being broken and formed. Only then can we be sure to obtain accurate barrier heights and bond energies. The modern methods of QM (generalized valence bond (GVB) [1], pseudo spectral generalized valence bond (PS-GVB) [2], multi-reference configuration integral (MR-CI) [3], and (gaussian dual space density functional theory (GDS-DFT) [4]) can give accurate barriers for reactions useful in studying the properties of nanoscale materials. However, despite the progress in first principles electronic structure theory, the calculations are often far too slow for studying the dynamics of polymers applications. This is necessary to have general approaches for averaging the electrons from QM to obtain an FF in terms of atomic positions. For finite molecules; A new methodology (PS-GVB) combining pseudo-spectral (PS) multi-grid and de-aliasing strategies with the sophisticated many-body wave functions [generalized valence bond (GVB)] were implemented and applied to large scale problems. PS-GVB led to considerably better scaling with size (N^2 rather than the N^3, N^4, N^5, N^6 characteristic of alternative methods) and simpler

parallelization. PS-GVB has been extended to treat all atoms of the periodic table (using core effective potentials), handle new sophisticated wave functions (GVB-RCI, MP2), and describe important properties (solvation energies, reaction rates, activation/reaction barriers). We will optimize these methods for parallel implementations, and extend the methodology to include GVB-RCI-MP2 and self-consistent GVB-RCI.

2.1.2. Density functional theory applications

Most practical materials properties require a description of infinite systems using periodic boundary conditions (PBC). This is three-dimensional (3D) for bulk properties or two-dimensional (2D) for surface growth and interfaces. For this purpose, we have developed a new method, Gaussian dual space density functional theory (GDS–DFT), in which most parts scale linearly with N. In implementing this, we have developed a new separable pseudo-potential that can be applied to all atoms of the periodic table. We reformulated the theories for electronic structure calculations of periodic systems in a way suitable for large-scale calculations using Gaussian basis functions. An accurate grid is introduced for efficient calculation of matrix elements. A dual-space approach is used to calculate the Coulomb potential with computational cost that scales linearly with the size of basis set. Preconditioned generalized conjugate gradients approach is introduced for rapidly converging wave functions expressed in terms of Gaussian basis functions. This method is applied to a variety of systems with excellent results.

2.2. Force fields (FF)

Using quantum mechanical results we develop FF descriptions to provide the energetics needed for the simulations of the nano-phase materials and their properties. The FF must even be accurate enough to obtain the proper energy differences for representing phase behavior of the materials and transferable so that one can apply it to phase transformations and interface phenomena. Standard FF generally uses simple springs to represent bonds and angles in describing structures and vibrations of molecules. Generally this is not sufficiently accurate to obtain a FF that accurately describes the properties of a specific class of molecules or polymers. For better FF, we fit to the QM using the Hessian-Biased FF (HBFF) [5] approach, which combines normal mode information from HF theory with the frequency information from theory or experiment. This HBFF approach has been used to develop accurate FF for polymers (e.g. PE, PVDF, nylon, POM, SiH) [6–10], ceramics (e.g. Si_3N_4, C_3N_4), [11,12] semiconductors [13] and metals [14].

On the other hand, for fast qualitatively considerations of new systems, we find that generic FF suitable for general classes of systems are most useful. DREIDING FF [15] (for the main group elements) and the Universal force field (UFF) [16] (all elements, including inorganics and organometallics) are such FF.

In recent years we made critical advances made in developing ab QM based FF for describing

(a) metals where many-body interactions play critical role on their physical properties; [17–21]
(b) oxides, ceramics, and zeolites where competition between ionic and covalent bonding is often very important, especially in describing polymorphic phase transitions, reactions, surface and interface properties; [22–24]
(c) covalent bonded systems such as carbon, hydrocarbons, silicon, germanium and their behavior far from equilibrium where the description of bond breaking and forming must be a part of an accurate classical description [25,26].

2.3. Molecular mechanics and molecular dynamics: MPSim

Using these FFs in large-scale MD simulations allows practical calculations on up to several millions of atoms. Our objective is to develop new strategies and algorithms in addition to taking advantage evolving hardware and software technologies to extend the time and distance scale to 100s of ns and close to microns. This will involve using fast multi-pole techniques, multiple time step approaches, NEIMO (Newton Euler inverse mass operator) method, CFA (constrained force algorithms) method, hyper MD approaches where they are suitable.

The focus here is on extending the methods of MD to physical systems of molecules, polymers, liquids, and inorganic materials with up to 100 million atoms while accurately treating long-range interactions using the cell multipole method (CMM). For fast internal coordinate dynamics on a million atoms, we have developed the NEIMO method. This methodology handles periodic systems and will be extended (Gibbs-Ensemble MD. The applications for this method will enable us to investigate the long time dynamics of liquid polymer and solid interfaces; which has tremendous impact on broad range of technological applications; such as wetting, adhesion, phase separation, coatings.

In MD simulations, the FF is used to predict the equations of motion. This leads to trajectories $[x_i(t), v_i(t), \ldots = 1, \ldots, 3N]$ that can be analyzed (using statistical mechanics and thermodynamics principles) to obtain macroscopic properties. MD simulations of heterogeneous nano-phase materials may require millions of atoms to be considered explicitly (a 25 nm cube of polyethylene has 1 million atoms). The most time-consuming aspect of the MD simulations of large systems is the accurate evaluation of the long-range interactions (electrostatic and dispersion), which decrease slowly with distance. Without cutoffs, this cost scales as order (N^2) for N particles (a system of 10 million atom leads to 10^{14} terms to be evaluated each step). Using cutoffs may reduce the computational cost. However, the cutoffs can lead to excessive errors. For a

periodic system, the Ewald procedure leads to accurate summations for these interactions, but the problem scales as $N^{1.5}$, totally impractical for systems with million atoms [27,28]. In order to simulate systems with millions of atoms, we developed methods and optimized parallel computer programs efficient for high capacity MD with the following advanced features:

(i) *Cell multipole method* [29] (CMM) which dramatically reduces the cost of long-range Coulomb and van der Waals interactions while retaining high accuracy. The cost scales linearly with size, allowing atomic-level simulations for million atom systems [30–33].
(ii) *Reduced cell multipole method* [34] (RCCM) which handles the special difficulties with long-range Coulomb interactions for crystals by combining a reduced unit cell plus CMM for interactions between the unit cell with its adjacent cells. The cost scales linearly with size while retaining high accuracy, allowing simulation of crystals having a million atoms per unit cell (the major use is for models of amorphous and semi-crystalline materials).
(iii) *Newton Euler inverse mass operator method (NEIMO)* [35–37] for internal coordinate dynamics (e.g. treats torsions only). This allows the solution of the dynamical equations for internal coordinates without inverting the mass tensor (moment of inertia tensor). The cost of NEIMO is linear in the number of degrees of freedom and small compared to other costs for million atom systems. More recently, we also developed a new constrained force algorithm (CFA) for massively parallel MD simulation of polymers and dendrimer [38,39].
(iv) *Advanced MD* algorithms to simulate systems under constant temperature and constant pressure conditions [40,41].
(v) *Nonequilibrium MD* We have implemented synthetic equations of motions to simulate various nonequilibrium conditions to predict transport properties such as viscosity, thermal conductivity of materials [42–45]. Using these methods, we have studied the effect of molecular topology of liquid alkanes on their measured viscosity indices [46,47].
(vi) *Steady state MD* Methods are used to simulate nonequilibrium processes such as friction and wear in nanoscopically confined lubricants and diamond surfaces. Here, the external work is dissipated through the material and coupled to a thermal bath using the Langevin equation [48–52].

2.4. Continuum solvent approaches

Solvents can have a major effect on the structure and properties of polymers. Consequently, we must include the solvent in the MD simulations. The costs are significant. For instance, in studying the Frechet Stimuli-responsive dendrimer our simulations included ~1609 atoms of the dendrimer plus ~80,000 atoms of solvent. Such explicit solvent calculations are compute-intensive and we have searched for accurate ways to obtain an implicit description of these solvent effects. In the biological literature, it is common to ignore the solvent and to modify the coulomb interactions between the atoms of the proteins by using a distance dependent dielectric constant. This is too crude for our purposes. Instead, we replace the solvent with a continuum solvent, the Poisson–Boltzmann approximation [53]. This approach provides a solution for large-scale solvation problems. It includes local solvent reorganization using explicit first solvation layer. This PB continuum solvation description serves as an intermediate step between implicit and explicit solvent simulations. We have used this the continuum solvent approach to study various polymers and biopolymers. Although the PB approximation greatly decreases the cost of accurate solvation, the PB calculation is still the expensive component of force evaluation in each MD step. Consequently, we are currently using another promising approach generalized Born (GB) method, in our MD simulations [54].

3. Applications

3.1. Multiscale modeling of biopolymers

Multi-scale modeling techniques are very vital to research problems in biology. From the fine level calculation of accurate binding energies for drug molecules using QM to coarse level structure prediction for proteins (both globular and membrane) and understanding viral protein coat assembly are some of the typical cases that require multi-scale modeling for biological systems. Such modeling schemes are also critical in bioengineering problems that offer excellent control in growth of a self-assembly at nanoscale. We have developed methods using CCBB MC [55,56] to predict the structure of globular proteins [57–59] and transmembrane proteins (G-protein coupled receptors). We have used this method to predict the structures of odor receptors in mammalian olfaction system. To understand the molecular basis of odor recognition we need to have an atomic level model of these odor receptors.

3.1.1. Multi-scale modeling techniques for deriving the atomic level structure of odor receptors

Odor receptors are seven helical domain membrane proteins that belong to the family of G-protein coupled receptors. We have used a combination of hydrophobicity profile prediction methods [60,61] and large-scale coarse grain MD methods with proper description of differential solvent environment to derive the atomic model for odor receptor OR S25. The protocol used for the multiscale modeling is shown in Fig. 2

Prediction of helical regions using hydrophobicity profiles and optimization: The *trans*-membrane helices

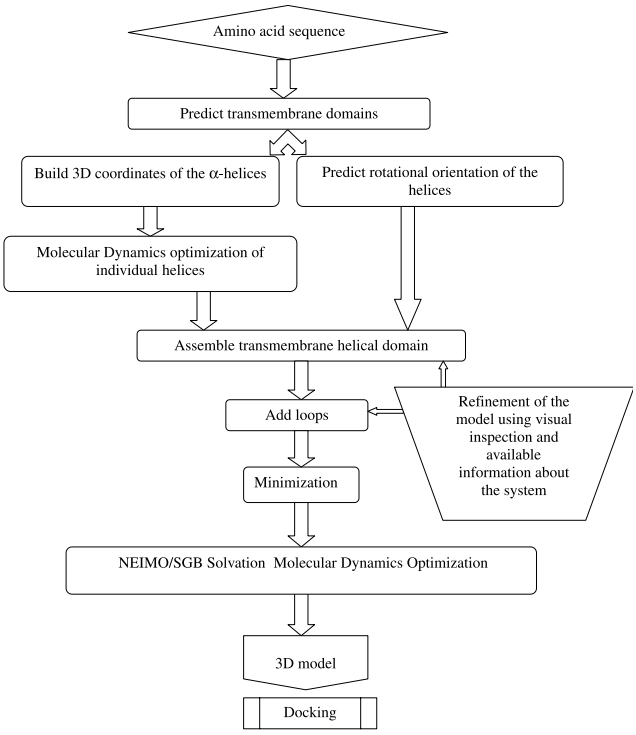

Fig. 2. Modeling strategy for odor receptors.

were identified on the basis of hydrophobicity by the multisequence profile method of Donelly et al. [60], as implemented in PERSCAN. The sequence used for ORS25 was used from the data by Malnic et al. [62]. For validation, the analysis was done on 21 rat olfactory receptors reported by Singer et al. [61]. Sequences were aligned by the iterative profile alignment utility of WHATIF [63]. The sequence from Ref. [62] was used for the odor receptor S25 to build canonical right-handed α-helices with Builder and Homology software (MSI). The structure of the helices thus built were optimized using NEIMO torsional MD method [35,36]. NEIMO algorithm is a fast torsional dynamics method that scales linearly with the number of torsional degrees of freedom.

Helix assembly: Helical rotations and the orientations of the helical axes were built using the bovine rhodopsin 7.5 Å electron density map [64]. We found that the proper description of the membrane bilayer is critical to packing the helices using rigid body MD. Dreiding FF [15] was used for the hydrophobic tail of the lipids. The charges on the polar heads of the lipids were assigned using the charge equilibration scheme. Crystal simulations of the lipid bilayer at constant pressure and temperature were performed using the PBC. These simulations reproduced the experimental crystal cell dimensions and density accurately. Following the assembly of the helices in the transmembrane domain, we performed 200 ps of rigid body dynamics of the helices with a barrel of lipid surrounding the helical barrel. For the protein Dreiding FF with charges from CHARMM [65] was used.

Optimization of the full atomic model: Following the rigid body dynamics described in Section 3.1 we further added the loops to the helices according to the sequence given in Malnic et al. [62] Loops were added using WHATIF [63] software. Following the addition of loops we performed a

Table 1
Carbon alpha root mean square (C_αCRMS) deviation for the modeled bacteriorhodopsin structure after MD compared to the crystallographic structure

	BRDP structure	C_αCRMS (Å)		
		Helices[a]	Loops[b]	Complete[c]
Xtal	Crystallographic structure (xtal)[d]	0.0	0.0	0.0
Modeled	Modeled helix bundle (raw) [e]	3.16		3.15 (163 aa)
Helix	Modeled helix bundle minimized[f]	3.29		3.28 (163 aa)
Bundle	Modeled helix bundle after 180 ps RBMD at 300 K[g]	3.32		3.31 (163 aa)
	Complete model (raw)	3.32	7.22	4.62 (221 aa)
Complete	Complete model (minimized DPG)[h]	3.30	7.41	4.69 (221 aa)
Model	Complete model after 50 ps of NEIMO/SGB TVN[i]	3.29	8.57	5.98 (221 aa)

[a] *Helices* refers to residues (aa) in the initial helix bundle (residues predicted as helical) compared to the corresponding region of the crystallographic structure (see text for the predicted transmembrane regions) (162 residues).
[b] *Loops* refers to inter helical regions that were not predicted as helical compared to the crystallographic structure (55 residues).
[c] *Complete* compares the corresponding complete structure to the crystallographic one.
[d] The crystallographic (xtal) structure corresponds to pdb code 2brd (resolution 3.5 Å), without residue Ala228 (which had missing atoms).
[e] *Raw* refers to model before any molecular mechanics (MM) or dynamics (MD) calculation.
[f] This is a raw model after conjugate gradient minimization in vacuum, in presence of Sodium Diphosphatidylglycerophosphate (DPG) bilayers.
[g] RBMD is Rigid Body MD with DPG bilayers.
[h] The complete model was minimized in the presence of DPG bilayers.
[i] Newton–Euler Inverse Mass Operator (NEIMO) method with H-NEIMO for protein. SGB (Surface Generalized Born) approach for solvation with a dielectric constant of 60. This was done with helices treated using H-NEIMO and loops with NEIMO, the counterions as Cartesian atoms. The membrane was simulated by a ring of DPG bilayers that were kept as rigid bodies.

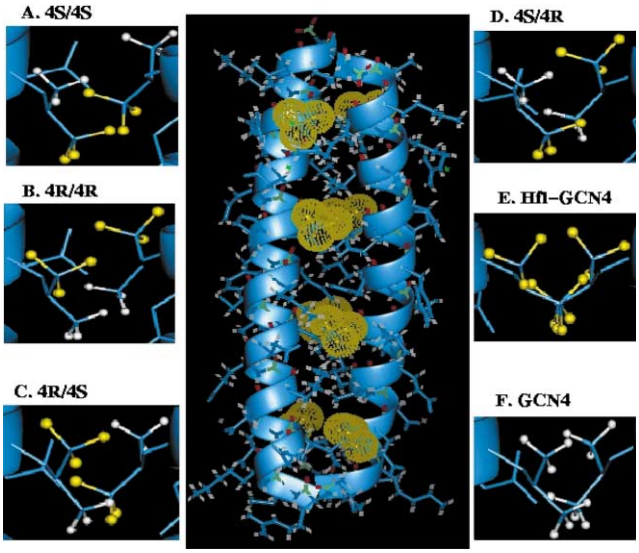

Fig. 3. The trifluoroleucine subsituted gcn4-pl leucine zipper is shown in the center. Possible configurations of the leucine/trifluoroleucine stereocenter at the γ-carbon on trifluoroleucine. Shown here are the various packing possibilities considered in the MD simulations. (A) 4*S*/4*S*, 'close'; (B) 4*R*/4*R*, 'far'; (C) 4*R*/4*S*; (D) 4*S*/4*R*; and (E) Hfl/Hfl(Hfl-GCN4); (F) Leu Leu(Gcn4), where both leucines are substituted with hexafluoroleucine.

full minimization of all the atoms with a barrel of lipid surrounding the protein. Counterions Na^+ and Cl^{-1} were added to neutralize acidic and basic residue side chains. The outside of the lipid layer was simulated using a continuum solvent description model (the surface generalized Born model [66]). A dielectric of 60.0 was used to simulate the low dielectric region surrounding the membrane. To optimize the solution structure further we then performed a multiscale mixed mode dynamics. The helices and loops in the protein were modeled using the NEIMO torsional MD, the lipids were treated as rigid bodies and the counterions as free Cartesian atoms. Constant temperature mixed mode dynamics yielded an optimum model for the atomic structure.

Control simulations: Our protocol described above was first tested on bacteriorhodopsin, a membrane protein for which the crystal structure has been fitted with fair accuracy in the transmembrane region of the protein. We started from the sequence of bacteriorhodopsin, used no knowledge of the crystal structure, and built the complete model using the above protocol. The overall RMS deviation in coordinates of C_α atoms for the final model is 5.98 Å for all the 221 amino acids. The CRMS for the residues in the membrane barrel is 3.29 Å while that for the loops is 8.57 Å. It is seen from Table 1 that the multiscale modeling improved the model by making the loops more flexible and defining the helical regions consistently. Thus, this modeling procedure gives a very reasonable model for a known membrane protein. Having evaluated the control protein, we further used the same protocol for modeling olfactory receptors.

Modeling of S25 olfactory receptor: The odor receptor S25 from Malnic et al. [64] has odor detection responses only to alcohols and not the other acids tested. We built the model using the sequence for S25 from Malnic et al. [64] and the procedures described above. The membrane is simulated using explicit lipid bilayers of Dilauroylphosphatidyl choline (DPC). The choice of lipid in the OR case is supported by experimental indications that the membrane surrounding the ORs in vivo can be satisfactory simulated using a single component lipid system of DPC. The final atomic level model used in further docking studies is showed in Fig. 3. Using the HEIR-Dock protocol [67–69] we have predicted the binding site for alcohol and acid odorants in ORS25. This dynamic receptor structure not only points to a likely odor-binding site but also independently predicts the two compounds that experimentally best activate ORS25. The results provide a mechanistic model for olfactory transduction at the molecular level and show how the basic GPCR template is adapted for encoding the enormous odor space.

3.1.2. Stabilization of leucine zipper coiled coils by introduction of trifluoroleucine [70]

Engineering of stable enzymes and robust therapeutic proteins is of central importance to the biotechnology and pharmaceutical industries. Although protein engineering provides powerful tools for the enhancement of enzymatic activity and protein stability, the scope of in vivo engineering methods is limited by the availability of just 20 naturally occurring proteinogenic amino acids. Increasing success in the incorporation of non-canonical amino acids into recombinant proteins in vivo has allowed the introduction of novel side-chain functionality into engineered proteins. This raises prospects of new approaches to the design of peptides and proteins of enhanced activity and/or stability. The effect of flourination of the side chains of substitution of leucine residues by 5,5,5-trifluoroleucine at the d-positions of the leucine zipper peptide GCN4-p1 increases the thermal stability of the coiled-coil structure [70]. To determine the origins of the stabilizing effect of side-chain fluorination, we carried out MD calculations using a continuum description of the solvent (Ref. [66]). A good description of solvent is critical to the simulation of biological systems. While using explicit solvent molecules in the simulation is computationally tedious Ghosh et al. [66] and Tannor et al. [2] have recently derived continuum solvent models that describe the solvent reaction field fairly accurate. In this study, we have clearly shown that the effect of solvation is well described both quantitatively on the binding energies and the structure prediction for fluorinated leucine zippers.

The MPSIM MD program and the DREIDING FF were used for all calculations. The starting structure for the Leu-GCN4-p1 dimer was taken from the RCSB Protein Data Bank. The fluorinated dimers were derived from the native dimer structure by replacement of the appropriate methyl hydrogens with fluorines, followed by re-optimization of the structure. Because the γ-carbon of trifluoroleucine (TFL) is asymmetric, multiple arrangements of adjacent diastereotopic

Table 2
Binding energies (BE, kcal/mol) of Leu-GCN4-p1 and fluorinated dimers. BE is the difference in the potential energy (averaged over 800 ps of MD after equilibration) of solvated monomers and the solvated dimer each from separate SGB MD calculations (final solvation energies with PBF). BE is quoted per mole of the monomer. % increase is the increase in BE compared to the Leu-GCN4-p1 structure. Also shown is the % helicity of each

Structure	BE	Increase (%)	Helicity (%)[a]
Leu-GCN4-p1	65.08	0	90.8
Close (4*S*,4*S*)[b]	93.75	44	84.3
Far (4*R*,4*R*)	98.14	51	79.4
Mixed (4*S*,4*R*)	99.20	52	81.1
Mixed (4*R*,4*S*)	111.15	71	89.3
Tfl-average	100.56	55	83.5
Hfl-GCN4-1p	77.21	19	78.5

[a] Helicity quoted here has been calculated as the ratio of the residues with torsion angles ϕ and ψ in the helical region of the Ramachandran plot to the total number of residues in the protein.

[b] Close, Far, Mixed: configuration of the pair of trifluoromethyl groups as shown in Fig. 3. Tfl-average: the averaged binding energy of the four configurations.

trifluoro-methyl groups must be considered (Fig. 3). When both Tfl residues at a given d-position are of the (2*S*,4*S*) configuration, the two trifluoromethyl groups are relatively close to one another; the fluorinated carbon centers are separated by ca. 6 Å. On the other hand, when two (2*S*,4*R*) isomers are juxtaposed, the corresponding carbon–carbon distance increases to about 8 Å. The trifluoromethyl groups are separated by intermediate distances, in the remaining configurations (where the two strands carry different isomers). We performed simulations on all configurations, to determine how side-chain stereochemistry affects dimer stability. For each dimer we carried out 1 ns of constant temperature (300 K) Nose–Hoover MD with the SGB description of the water solvent.

From the 1 ns trajectory, we calculated the average properties over 800 ps after equilibration. The binding energies were calculated as the difference in potential energies of the solvated dimer and the corresponding solvated monomers. Table 2 reports the average values of the binding energy (per monomer) for the native and fluorinated forms.

The Tfl-GCN4-p1 dimers are predicted to exhibit binding energies (Table 2) ca. 55% larger than that of the leucine form (calculated relative to the respective random coil monomers). The various stereochemical arrangements lead to increases ranging from 44 to 71%, indicating that side-chain configuration may have some differential effect on dimer stability. This is in excellent agreement with the experimentally measured free energy difference between Tfl-GCN4-p1 and GCN4-pl which is 57%. Similar analysis of a hexafluoroleucine (Hfl) dimer leads to the prediction that such dimers (which were not prepared experimentally in this work) would be less stable than the Tfl dimers but marginally more stable (19%) than the wild type.

To investigate the source of stability of the fluorinated dimers we analyzed the components of the binding energy for each peptide. The primary driving forces for stabilizing the Tfl-GCN4-p1 dimers are predicted to arise from van der Waals (vdW) and hydrogen bonding interactions. Consideration of electrostatic (intra- and inter-peptide coulomb forces) and solvation interactions suggests a hydrophobic effect that favors burial of CF_3 rather than CH_3 in the dimer. If just coulomb and solvation interactions are considered, the driving force for dimerization is predicted to decrease in the order Hfl > Tfl > Leu. It is the balance of desolvation, electrostatics, H-bonding and vdW forces that leads to the prediction that the Tfl dimers are more stable than the Hfl dimer which is more stable than the native leucine dimer. The average helicities of dimers are predicted to be 90.8% for Leu-GCN4-p1, 83.5% for Tfl, and 78.5% for Hfl.

Our results demonstrate that the subtle change from four leucine methyl groups to four trifluoromethyl groups results in a large gain in stability of the folded structure. It is remarkable that the inclusion of the solvation effects predict the structures and binding energies between the two peptides with good accuracy.

3.2. Modeling polymer sensors for the electronic nose

The Lewis group at Caltech [71–74] has experimentally constructed a particular design of an electronic nose. Sensors are built with conducting leads connected through thin film polymers loaded with carbon black. Odorant detection relies on a change in electric resistivity of the polymer film as function of the amount of swelling caused by the odorant vapor. The amount of swelling depends upon the chemical composition of the polymer and the odorant molecule. An array of 20 carbon black loaded polymers give rise to a specific change in resistivity patterns upon exposure to a given molecular species. The pattern is unique and unambiguously identifies the compound [73,74].

It is of great value to be able to correlate from first principles the change of resistivity of a given polymer sensor with the chemical nature of the solvent. Predictions of this type may be of practical use for increasing the electronic nose sensitivity for specific compounds such as those found in the wine, cheese or perfume industries, or for detecting nerve gases and air bound compounds emanating from explosives. Here we report a molecular modeling method that provides a strong correlation between the calculated properties of a series of polymers and solvents and the experimental relative change in the resistivity of the sensors upon exposure to these solvents.

3.2.1. Method

The permeability of a solvent in a polymer is related to the heat of sorption as follow [75]

$$P = P_0 \exp(-\Delta E_s/RT) \exp(-\Delta H_s/RT) \quad (1)$$

P_0 is the exponential pre-factor related to entropy, ΔH_s is

the heat of sorption of the solvent in the polymer, and E_s is the activation energy for diffusion of the molecule in the polymer. Because the amount of swelling at a fixed time is proportional to the permeability of the polymer towards the solvent, the change in resistivity, $\Delta R/R$, could be modeled with an expression similar to Eq. (1). A computational method for the estimation of the heat of sorption, or other strongly correlated property, would be valuable.

Hansen [76,77] proposed an extension of the Hildebrand parameter method to estimate the relative miscibility of polar and hydrogen bonding systems

$$\delta^2 = \delta_d^2 + \delta_p^2 + \delta_h^2 \tag{2}$$

Where δ corresponds to the Hildebrand solubility parameter,

$$\delta^2 = \Delta H_v / V_m \tag{3}$$

The two quantities are not expected to be identical any more than the Hildebrand parameters of liquids with specific interactions are identical when determined by different methods. ΔH_v is the heat of vaporization and V_m the molar volume. The Hansen solubility parameters in Eq. (2) are determined empirically based on many experimental observations. Here we introduced a new modeling method to estimate Hansen solubilities. Furthermore, we use the predicted Hansen enthalpies $H_i = V_m \delta_i^2$ of the polymer and solvent molecules to construct a model for the change in relative resistivity

$$\Delta R/R = R_0 \exp(-\gamma V_k/RT) \exp\left(\sum \beta_i [H_i^{(k)} - H_i^{(n)}]\right) \tag{4}$$

Where $\Delta R/R$ is the change in resistivity upon exposing polymer sensor n to odorant k, R_0 is sensor's resistivity in air. $H_i^{(k)}$ and $H_i^{(n)} (i = 1, 2, 3)$ *are* the three components (electrostatic, dispersion, and hydrogen bond) of the solvent and polymer Hansen enthalpies, respectively. These components are calculated using first principles MD in a suitable FF [15,16]. $\Delta E_k = \gamma V_k$ is a diffusion barrier directly proportional to the molecular volume of the solvent. This relation follows from the fact that the diffusion coefficient is linearly related to the molar volume of the penetrant, particularly when the temperature is greater than the glass transition (T_g) of the polymer [78].

3.2.2. Hansen parameters from MD simulations

A precise method was developed to estimate the Hansen solubilities of solvents and polymers from MD calculations under PBC. The procedure has been coded as a single application under the Software Developer's Kit (SDK) distributed by MSI [79]. A unit cell of twelve solvent molecules (or four polymer chains) is built at 50% of the target density. This step is accomplished with the amorphous builder in the Cerius2 software package [80] with a Van der Waals radius-scaling factor of 0.30. If available the experimental density of the solvent or polymer are used as a target value, although the final density may differ slightly depending on the FF employed. The charges of the isolated solvent or polymer molecules were based on the charge equilibration method [81] and the rest of the parameters were taken from the Dreidiing forcefield [15]. The potential energy of the bulk system is minimized for 5000 steps or until the atom rms force converges to 0.10 kcal/mol Å. 750 steps of MD (1 fs/step) at a temperature of 700 K using canonical fixed volume dynamics (TVN) is carried out to anneal the sample. The cell is then minimized with the previous procedure. The reduced cell coordinates are shrunk such that the density is 64% of the target density. The atoms' coordinates are minimized and dynamics is done on the system with the previously described procedure holding the cell fixed. A total of five compression, dynamics, and minimization cycles are performed until the density reaches 120% of the target density. Then the cell parameters are increased in five reverse cycles of expansion, dynamics, and minimization until the target density is reached. Finally, the sample is allowed to relax in a minimization involving the cell and the atoms' coordinates. The Hansen enthalpy components are calculated by subtracting the potential energy of the bulk system from the sum of the potential energies of the individual molecules separated at an infinite distance. This process is repeated ten times with different initial random packing. Hansen solubility parameters and molar volumes were computed as well as the standard deviations. In polymer calculations, the number of monomers in each chain was determined such that the total volume of the four chains was approximately 5900 Å^3. The initial polymer amorphous structures were constructed using a one-dimensional rotational isomeric states (RIS) approach to achieve a correct distribution of conformational states.

3.2.3. Results and discussion

The experimentally determined relative resistivity of seven polymer sensors upon exposure to twenty-four solvent vapors was correlated with the calculated Hansen enthalpy components and molar volumes via Eq. (4). The correlation is shown in Fig. 4 for seven electronic nose polymer sensors and 24 solvents.

Strong linear correlations (Table 3) between the experimentally determined [82] change in resistivity and the permeability-related expression Eq. (4) were found for seven different polymer sensors (polymethylmethacrylate

Table 3
Pearson R correlation values and slopes of predicted versus experimental $\Delta R/R$ for each of seven polymer odorant detectors

Polymer sensor	Slope	R
Polycaprolactone	0.858	0.925
Polysulfone	0.932	0.962
PMMA	0.678	0.827
PEVA	0.888	0.936
Polyethylene	0.870	0.933
Polyethyleneoxide	0.746	0.874
4-HydroxyPS	1.018	0.991

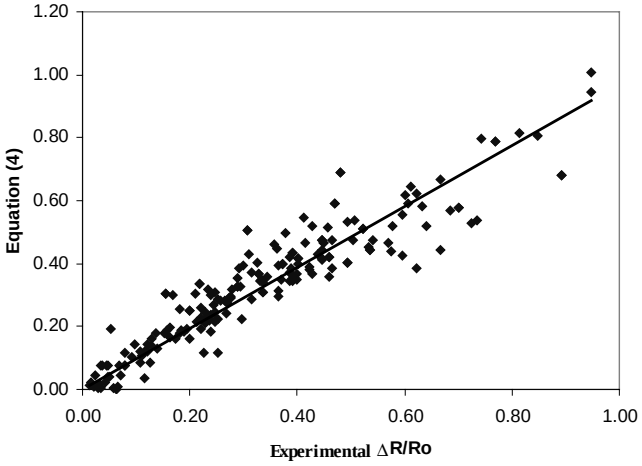

Fig. 4. Correlation between modeled and experimental changes in resistivity of seven polymer sensors exposed to 24 solvents.

(PMMA), 4-hydroxypolystyrene (4HPS), polyethyleneoxide (PEO), polyethylene (PE), polyethylenevinylacetate (PEVA), polysulfone, and caprolactone). Eq. (4) fitting parameters for the various polymer sensors are given in Table 4. Calculated densities and Hansen solubilities for the seven polymers and 24 solvents are summarized in Table 5.

The slopes and the Pearson R values for the correlation plots are listed in Table 4. The correlation was particularly good for polysulfone, 4-hydroxypolystyrene and PEVA (polyethylene-*co*-vinyl acetate) and especially poor for polymethylmethacrylate based on both correlation slope and the Pearson R values for the linear fit. Polysulfone appears to discriminate between solvents of different sizes since the free volume fraction is small and the free volume distribution may be narrow, resulting in a 'molecular' sieve effect. Additionally, the experimental relative change in resistivity in polysulfone ranges from zero to 1.0, which makes it a particularly good high-resolution sensor.

The polyethylene-*co*-vinyl acetate detector also correlates reasonably well with the theoretical relative change in resistivity. However, the relative change in resistivity range is smaller compared to polysulfone indicating that it is less discriminating towards ester and alcohol solvents. A possible explanation that accounts for this observation is that PEVA contains polar ester functional groups due to the vinyl content (18%), as well as non-polar components due to the polyethylene content (82%). PEVA has a glass transition below room temperature and as a result contains a large free volume fraction. This decreases the sensitivity towards molecules of different sizes compared to high T_g polymers such as polysulfone. The third particularly good detector in terms of signal correlation with theoretical prediction is 4-hydroxy-polystyrene. This detector is particularly sensitive to molecules functionalized with highly polar groups such as alcohol, obviously due to the hydroxyl functional group. However, the sensitivity of this sensor to moderately polar or non-polar solvents such as esters is particularly low.

3.3. Diffusion of gases in amorphous polymers

The diffusion of molecules in polymer matrices involves mesoscale times [microseconds (μs) to seconds (ms)], far too long for routine MD simulations [83–86]. Consequently we formulated the Monte Carlo Void Diffusion (MCVD) method to calculate diffusion of gases in polymer matrices for very long time scales based on coarse-grained information extracted from short [sub nanoseconds (ns)] MD simulations. The MD (over ~200 ps) is used to define a probability of having a void at each point of a grid. The MCVD considers random motion of a penetrant molecule on this grid. We show that the MC and MD both give rise to an anomalous ($R^2 \propto t^{1/2}$) behavior at short time and Einstein diffusion behavior ($R^2 \propto t$) at long time. Comparing the MD and MC at short time (~200 ps) provides the corresponding time for the MCVD step. It is practical to carry out MCVD for mesoscale times (μs to s). This represents an example of how to connect dynamics from the atomistic scale to the meso scale. The results reported are on studies of the diffusion of He in an amorphous polyethylene (PE) matrix.

The permeability (P) of a gas through a membrane can be written as [87]

$$P = DS \tag{5}$$

where D is the diffusion coefficient and S is the solubility. Generally, only P is available experimentally, but D and S often depend differently on the various design parameters. The total distance (R) travelled in a time (t) is given by the Einstein relation

$$\left\langle R^2 \right\rangle = 6Dt \quad \text{as } t \to \infty \tag{6}$$

where $\langle\ \rangle$ designates averaging over the ensemble of starting

Table 4
Model parameters (Eq. (4)) for seven electronic nose polymer sensors

Model parameter		PMMA	4HPS	PEO	PE	PEVA	Poly sulfone	Capro-lactone
Pre-exponential	L_nR_0	0.676	0.233	−0.761	2.296	0.770	1.092	−0.813
Electrostatic	β_1	−0.001	−0.028	0.014	0.040	0.018	−0.001	0.019
Dispersion	β_2	0.007	−0.007	0.012	0.047	0.020	−0.007	0.031
Hydrogen bond	β_3	0.026	0.042	0.016	0.060	0.030	0.029	0.040
Diffusion	γ	0.009	0.033	0.003	0.011	0.007	0.012	0.006

Table 5
Estimated densities and Hansen solubilities

Solvents	Density (g/cc)	δ^2/V_m (Kcal/mol)	H_1 Electrostatic	H_2 Dispersion	H_3 H-bonding
2-Pentanol	0.89	−151.42	−53.32	−76.48	−21.62
3-Pentanol	0.88	−142.40	−47.89	−76.87	−17.64
Amylacetate	0.95	−127.31	−40.19	−87.13	0.00
Butylacetate	0.97	−132.03	−41.75	−90.28	0.00
Decylacetate	0.91	−104.70	−21.02	−83.68	0.00
Ethanol	0.88	−257.64	−146.00	−51.35	−60.29
Ethylacetate	1.01	−159.31	−68.99	−90.33	0.00
Hexylacetate	0.95	−122.55	−34.83	−87.72	0.00
Iso-amylalcohol	0.89	−159.46	−59.82	−73.87	−25.77
Isoamylacetate	0.96	−125.90	−38.67	−87.24	0.00
Isoamylbenzoate	1.03	−119.56	−23.04	−96.52	0.00
Isoamylbutyrate	0.94	−111.52	−25.34	−86.17	0.00
Isoamylcaproate	0.92	−104.57	−20.83	−83.74	0.00
Isoamylpropionate	0.93	−113.17	−30.36	−82.81	0.00
Isobutylacetate	0.96	−130.92	−45.05	−85.87	0.00
Isopropylacetate	0.98	−143.46	−57.20	−86.26	0.00
n-amylalcohol	0.88	−159.42	−59.53	−75.46	−24.44
n-Heptanol	0.87	−130.23	−37.63	−76.59	−16.01
n-Hexanol	0.88	−141.38	−46.42	−77.97	−16.99
n-Propanol	0.86	−193.82	−94.68	−60.77	−38.37
Octanol	0.88	−127.59	−33.80	−79.91	−13.88
Octylacetate	0.92	−112.37	−26.42	−85.95	0.00
Propylacetate	0.98	−142.96	−54.90	−88.06	0.00
n-Butanol	0.84	−152.72	−64.31	−61.58	−26.82
Polymers					
PMMA	1.11	−90.51	−31.19	−59.32	0.00
4HPS	1.09	−106.66	−28.66	−64.48	−13.51
PEO	1.13	−168.10	−68.36	−95.90	−3.84
PE	0.88	−85.45	−1.00	−84.46	0.00
PEVA	0.96	−85.02	−10.82	−74.20	0.00
Polysulfone	1.30	−138.74	−29.76	−108.98	0.00
Caprolactone	1.09	−122.66	−35.31	−87.34	0.00

and ending points for the given time interval t. To predict D for a He in PE, we perform a number of MD calculations, each starting with He in various sites, for times sufficiently long that Eq. (6) is obeyed.

An example is given in Fig. 5a below on the left of He diffusion in PE. Here we see that 1.5 ns of MD leads to the behavior in Eq. (6). Hence, the MD can be used to determine D. The Fig. 5b on the right shows that for O_2 in a PVC/PVDC copolymer, 1.5 ns of MD is not sufficient to display Einsteinian diffusion, and we estimate that this latter case requires a μs time scale.

Fig. 6 shows the trajectories for five He atoms diffusing for 1.5 ns in PE. There are three-dimensional regions (we call them *felicitons*) in which the gases spend significant times [≈ 20–70 picoseconds (ps)] separated by pseudo one-dimensional channels where they spend shorter times (≈ 5–20 ps). Calculations on various gas molecules (H_2, CO_2, O_2, He, Ar) diffusing in various amorphous polymers give similar results, suggesting that this *feliciton*-channel network is generally observed in MD.

Fig. 7 shows the dynamical void distributions in the polymer. Here we partitioned the unit cell into one million

Table 6
The MD to MCVD time constants

Temperature	D (Å^2/ps)	Time conversion (fs/MCVD step)			Ratio $t_{\text{anomalous}}/t_{\text{Fickian}}$
		Crossover	Anomalous	Fickian	
400	1.77	4.23	8.03	8.47	0.95
350	1.30	10.00	10.00	9.23	1.08
300	0.60	8.91	8.91	5.83	1.53
250	0.20	9.97	9.97	6.00	1.66
200	0.12	7.84	7.84	8.33	0.94

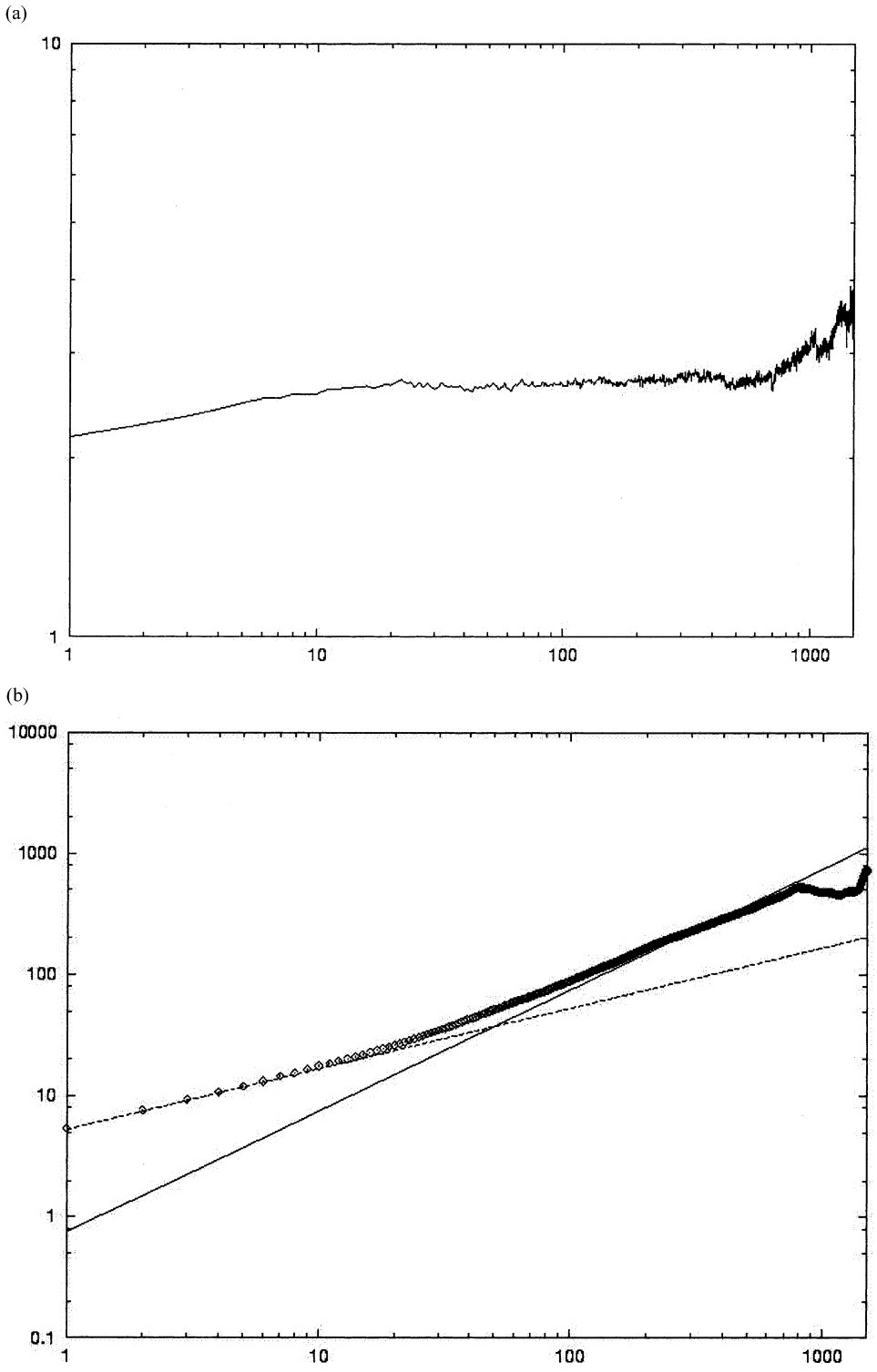

Fig. 5. (a) He diffusion in PE. Here we see that 1.5 ns of MD leads to the behavior in (2). Hence the MD can be used to determine D. (b) O_2 diffusion in a PVC/PVDC copolymer, 1.5 ns of MD is not sufficient to display Einsteinian diffusion, and we estimate that this latter case requires a μs time scale.

cells ($100 \times 100 \times 100$) and examined the voids over a period of 200 ps. Every 5 ps we examined whether a probe radius 0.7 Å would contact any part of the polymer. Here we see that the void analysis leads to an excellent match with the felicitons and channels defined by the gas particle in MD.

To calculate the mean square displacement (MSD) with time, we considered each ps step of the 10 ns trajectory to be

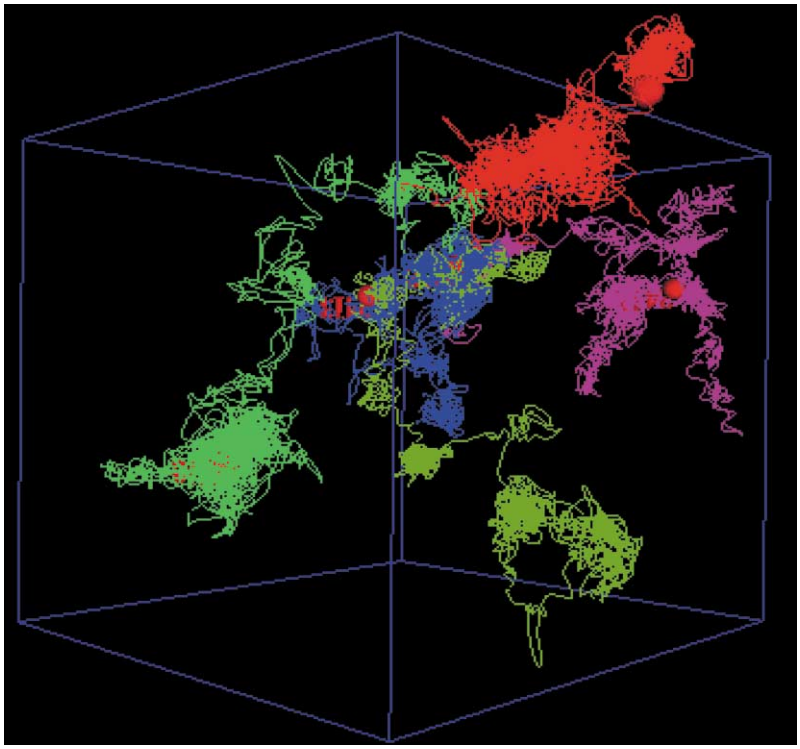

Fig. 6. The trajectories for five He atoms diffusing for 1.5 ns in PE.

a possible starting point

$$R_2(\tau) = \sum_{t_0=0}^{T-\tau} |R(t+\tau) - R(t_0)|^2 / \sum_{t_0=0}^{T-\tau} 1$$

where, T is the total time. To determine whether the system is in the diffusion region, where the Einstein relation Eq. (2) holds, we plot $\log\langle R^2\rangle$ vs. $\log t$. This should have a slope of unity with the intercept providing the value for $6D$. Indeed, Fig. 8 shows diffusive behavior for $\tau \geq 0.1$ ns averaged over all 5 He atoms. The intercept, $(6D)$, leads to $D = 1.77\ A^2/\text{ps} = 29.5 \times 10^{-6}\ cm^2/s$ ($\rho = 0.854\ g/cc$)./

The experimental diffusion coefficient [88] of He in LDPE ($\rho = 0.914$ g/cc) at 25°C is $D = 6.8 \times 10^{-6}$ cm^2/s and in HDPE ($\rho = 0.964$ g/cc) at 25°C is $D = 3.07 \times 10^{-6}$ cm^2/s. The lower density and lower MW in the calculations is consistent with the higher D.

Both from the MD and MCVD, we observe three regions:

- *Ballistic:* Up to ~0.03 ps, the distance increases linearly with time ($\langle R^2\rangle \propto t^2$). This is the *ballistic regime*, before the particle hits a wall of the *feliciton*.
- Anomalous: From ~0.25 ps to ~4 ps, the trajectory fits the $\langle R^2\rangle \propto t^{1/2}$ line quite well. This is the *anomalous diffusion region*, corresponding to intra-*feliciton* motion. During this time the motion is primarily within *felicitons*. We have found such anomalous diffusion regions in all studies of amorphous polymers.
- Fickian: For times longer than 0.1 ns we find true Einsteinian diffusion conditions.

Given the void probability grid from MD we design a random walk MC algorithm in which a particle on a grid point moves to an adjacent grid point. We assume the probability to be proportional to the void weight ($W_g = 1$ if always a void to $W_g = 0$ if never a void). In order for a random walk process to mimic this motion, we include a momentum bias in the jump probability with an angular dependence based on the last previous step direction. We find that a simple cosine term, of the angle between the last step and the next possible jump direction, leads to a MCVD trajectory within a *feliciton* that mimics the MD trajectory. A second issue concerns which neighboring points are allowed for the jump. Simple choices are:

(a) only the six nearest neighbor points (forward, backward, up, down, right, left),
(b) 18 points also including next nearest neighbors, or
(c) 26 points also including third nearest neighbors.

We chose case (c) since it efficiently spans the choices of solid angle, allowing channels in diagonal direction to be found.

The remaining issue concerns converting the MCVD step to physical time. We have considered three ways to do this:

(1) *Fickian match*: If MD for sufficiently long time is available (200 ps for He/PE and several ns for other combinations such as O_2/PVC-PVDC), then one can obtain the diffusion constant from the Fickian regime of the MD and use this to get the conversion from MC step

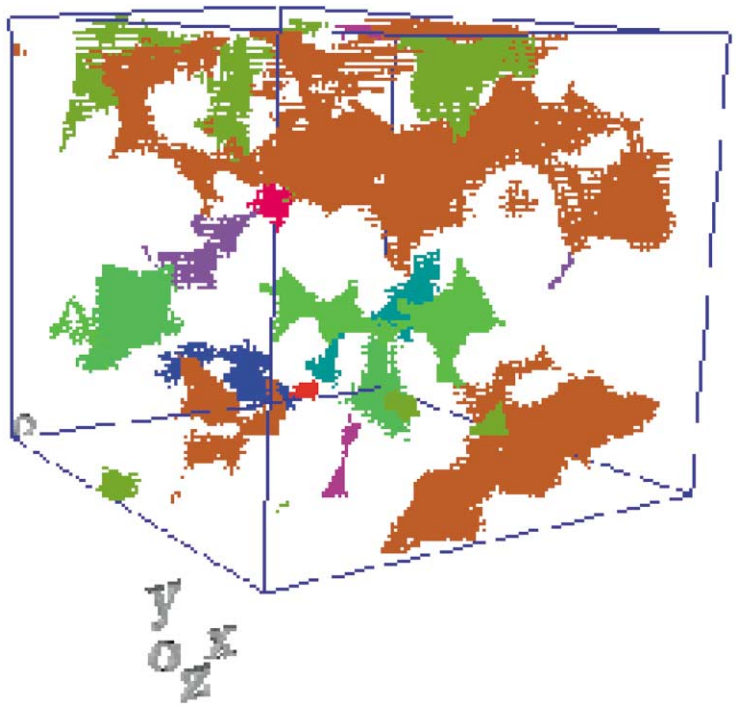

Fig. 7. The dynamical void distributions in the polymer.

to actual time. This corresponds to matching the log R^2 − log t intercepts for the Fickian regimes.

(2) *Crossover match*: If MD for less time is available (50 ps for He/PE), then one can match the crossover time from the anomalous to the Fickian regime and obtain the conversion from MC step to actual time.

(3) *Anomalous match*: For shorter time scales, or polymers where the crossover is not observed in MD, one can match the log R^2 − log t intercepts of the anomalous regime from MD and MCVD.

The anomalous match is preferred since it requires the least time for the MD simulations. Most polymer systems show a well-defined anomalous behavior within ps to ns MD time. However, the question is whether this corresponds to the conversion from the longer time MD. For He/PE the MD was sufficiently long to consider all three methods. Table 6 shows the MD to MCVD time constant for all 3 cases. We see that while the diffusion constant changes by a factor of 15 between the temperature extremes (1.77@400 K → 0.12@200 K)

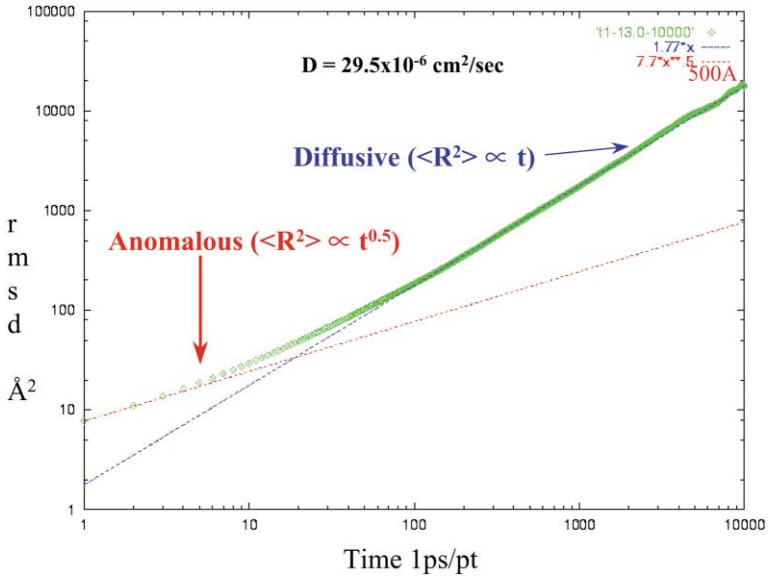

Fig. 8. The diffusive behavior for $\tau \geq 0.1$ ns averaged over all 5 He atoms. The intercept ($6D$) leads to $D = 1.77$ A^2/ps $= 29.5 \times 10^{-6}$ cm^2/s ($\rho = 0.854$ g/cc).

the time factor from the anomalous diffusion match differs only by 20%.

The research projects reported in this paper are supported by grants from DOE-ASCI, NASA/Ames, NASA-JPL, Owens Corning, Chevron Research Technology Co. Facilities of MSC is also supported by funds from NSF (CHE 95-22179), ARO/DURIP, ARO-MURI, ONR; Asahi Chemical, Avery Dennison, BP Chemical, Beckman Institute, Dow Chemical, Chevron Petroleum Technology Co., Chevron Chemical Co., Exxon, Kellogg, Seiko-Epson

References

[1] Goddard III WA, Dunning Jr. TH, Hunt WJ, Hay PJ. Accts Chem Res 1973;6:368.
[2] Tannor DJ, Marten B, Murphy R, Friesner RA, Sitkoff D, Nicholls A, Ringnalda M, Goddard III WA, Honig B. J Am Chem Soc 1994;116:11875.
[3] Greeley BH, Russo TV, Mainz DT, Friesner RA, Langlois J-M, Goddard III WA, Donnelly RE, Ringnalda MN. J Chem Phys 1994;101:4028.
[4] Chen XJ, Langlois J-M, Goddard WA. Phys Rev B 1995;52:2348.
[5] Dasgupta S, Yamasaki T, Goddard III WA. J Chem Phys 1996;104:2898.
[6] Karasawa N, Dasgupta S, Goddard III WA. J Phys Chem 1990;95:2260.
[7] Dasgupta S, Hammond WB, Goddard III WA. J Am Chem Soc 1996;118:12291–301.
[8] Karasawa N, Goddard III WA. Macromolecules 1995;28:6765.
[9] Karasawa N, Goddard III WA. Macromolecules 1992;25:7268.
[10] Dasgupta S, Brameld KA, Fan CF, Goddard WA. Spectrosc Acta A 1997;53:1347–63.
[11] Dasgupta S, Smith KA, Goddard III WA. J Phys Chem 1993;97:10891.
[12] Musgrave CB, Dasgupta S, Goddard III WA. J Phys Chem 1995;99:13321.
[13] Musgrave CB, Harris SJ, Goddard III WA. Chem Phys Lett 1995;247:359.
[14] McAdon M, Goddard III WA. J Phys Chem 1987;91:2607.
[15] Mayo SL, Olafson BD, Goddard III WA. J Phys Chem 1990;94:8897.
[16] Rappé AK, Casewit CJ, Colwell KS, Goddard III WA, Skiff WM. J Am Chem Soc 1992;114:10024.
[17] Cagin T, Qi Y, Li H, Kimura Y, Ikeda H, Johnson WL, Goddard III WA. In: Inoue A, Johnson WL, Liu CT, editors. Bulk metallic glasses, MRS Symposium Series 5541999. Warrendale, PA: Materials Research Society, p. 43–8.
[18] Kimura Y, Cagin T, Qi Y, Goddard III WA, submitted for publication.
[19] Strachan A, Cagin T, Gulseren O, Cohen RE, Goddard III WA, qEAM FF for Tanatalum, unpublished.
[20] Cagin T, Demiralp E, Goddard III WA. MRS Symp Proc 1998;492:287–92.
[21] Demiralp E, Cagin T, Goddard III WA. Phys Rev Lett 1999;82:1708–11.
[22] Huff NT, Demiralp E, Cagin T, Goddard III WA. J Noncrystal Solids 1999;253:133–42.
[23] Kitao O, Demiralp E, Cagin T, Dasgupta S, Mikami M, Tanabe K, Ono S, Goddard III WA. Comput Mat Sci 1999;14:135–8.
[24] Strachan A, Cagin T, Goddard III WA. Phys Rev B 1999;60:15084.
[25] Che JW, Cagin T, Goddard III WA. Theo Chem Acct 1999;102:346–54.
[26] Duin A, Goddard III WA, submitted for publication.
[27] Karasawa N, Goddard III WA. J Phys Chem 1989;93:7320.
[28] Chen ZM, Cagin T, Goddard III WA. J Comp Chem 1997;18:1365.
[29] Ding HQ, Karasawa N, Goddard III WA. J Chem Phys 1992;97:6.
[30] Lim KT, Brunett S, Iotov M, McClurg RB, Vaidehi N, Dasgupta S, Taylor S, Goddard III WA. J Comp Chem 1997;18:501–21.
[31] Iotov M, Kashihara S, Dasgupta SD, Goddard III WA, Diffusion of gases in polymers, unpublished.
[32] Iotov M, PhD Thesis, California Institute of Technology, December 1997.
[33] Miklis P, Cagin T, Goddard III WA. J Am Chem Soc 1997;119:7458.
[34] Ding H, Karasawa N, Goddard III WA. Chem Phys Lett 1992;196:6.
[35] Mathiowetz AM, Jain A, Karasawa N, Goddard III WA. Proteins 1994;20:227.
[36] Vaidehi N, Jain A, Goddard III WA. J Phys Chem 1996;100:10508.
[37] Fijany A, Cagin T, Botero AJ, Goddard III WA. Adv Eng Software 1998;29:441–50.
[38] Fijany A, Botero AJ, Cagin T. In: D'Hollander EH, Joubert G, Peters F, Trottenberg U, editors. Parallel computing: fundamentals, applications and new directions, 1998. p. 505–15.
[39] Gao G, Iotov M, Cagin T, Goddard III WA, MPSim97: massively parallel molecular dynamics simulation program, in preparation.
[40] Cagin T, Karasawa N, Dasgupta S, Goddard III WA. Mat Res Soc Symp Proc 1992:278–83.
[41] Cagin T, Goddard III WA, Ary ML. Comp Polym Sci 1991;1:241.
[42] Parrinello M, Rahman A. Phys Rev Lett 1980;45:1196.
[43] Parrinello M, Rahman A. J Appl Phys 1981;52:7182.
[44] Nose S. Mol Phys 1984;52:255.
[45] Nose S. J Chem Phys 1984;81:511.
[46] Yue Qi, Cagin T, Kimura Y, Goddard III WA, Shear viscosity of a liquid metal alloy from NEMD: Au–Cu, unpublished.
[47] Che J, Cagin T, Goddard III WA, Thermal conductivity of diamond from NEMD. J Chem Phys 2000;113:6888-6900.
[48] Cagin T, Miklis P, Goddard III WA, Effect of molecular topology on the shear viscosity: linear, star and hyper-branched alkanes, in preparation.
[49] Cagin T, Che J, Gardos MN, Fijany A, Goddard III WA. Nanotech 1999;10:278–84.
[50] Cagin T, Zhou Y, Yamaguchi ES, Frazier R, Ho A, Tang Y, Goddard III WA. In: Drake JM, Grest GS, Klafter J, Kopelman R, editors. Dynamics in small confining systems V, MRS Symposium Series 5431999. Warrendale, PA: Materials Research Society, p. 79–84.
[51] Zhou Y, Cagin T, Yamaguchi ES, Ho A, Tang Y-C, Goddard III WA, Dynamical shear studies of lubricant films confined to nanoscale separation between iron oxide surfaces covered with wear inhibitors, submitted for publication.
[52] Qi Y, Cagin T, Kimura Y, Goddard III WA, Glass formation and crystallization in Ni:Cu and Cu:Ag alloys. Phys Rev B 1999;59:3527–3533.
[53] Cortis CM, Friesner RA. J Comput Chem 1997;18:1570 (see also p. 1591).
[54] Still WC, Tempczyk A, Hawley RC, Hendrickson T. J Am Chem Soc 1990;113:6127.
[55] Sadanobu J, Goddard III WA. Fluid Phase Equil 1998;144:415.
[56] Sadanobu J, Goddard WA. J Chem Phys 1997;106:6722.
[57] Debe DA, Goddard III WA. J Mol Biol 1999;294:619.
[58] Debe DA, Carlson MJ, Sadanobu J, Chan SI, Goddard III WA. J Phys Chem B 1999;103:3001.
[59] Debe DA, Carlson MJ, Goddard III WA. Proc Natl Acad Sci 1999;96:2596.
[60] Donnelly D. Biochem Soc T 1993;21:36–9.
[61] Singer MS, Weisinger-Lewin Y, Lancet D, Shepherd GM. Receptors Channels 1995;4:141–7.
[62] Malnic B, Hirono J, Sato T, Buck LB. Cell 1999;96:713–23.
[63] Vriend G, WHATIF: a molecular modeling and drug design program, J Mol Graph 8 52–6.
[64] Schertler GFX. Eye 1998;12:504–10.
[65] Mackerell AD, Wiorkiewicz-Kuczera J, Karplus M. JAm Chem Soc 1995;117:11946–75.

[66] Ghosh A, Rapp CS, Friesner RA. J Phys Chem B 1998;102:10983–90.
[67] Floriano WB, Vaidehi N, Singer MS, Shepherd G, Goddard III WA. Proc Nat Acad Sci 2000;97:10712-6.
[68] Datta D, Vaidehi N, Floriano WB, Prasadarao N, Goddard III WA, 2000, in preparation.
[69] Wang P, Vaidehi N, Tirrell NA, Goddard III WA, 2000, in preparation.
[70] Tang Y, Ghiralando G, Vaidehi N, Kua J, Mainz D, Delgrado WA, Goddard III WA, Tirrell DA. Biochem 2001;40:2790-6.
[71] Freund MS, Lewis NS. PNAS 1995;92:2652–6.
[72] Severin EJ, Doleman BJ, Lewis NS. Anal Chem 2000;72:658–68.
[73] Doleman BJ, Lonergan MC, Severin EJ, Vaid TP, Lewis NS. Anal Chem 1998;70:4177–90.
[74] Lonergan MC, Severin E, Doleman BJ, Beaber SA, Grubb RH, Lewis NS. Chem Mater 1996;8:2298–312.
[75] Sato T, Hirono J, Tonoike M, Takebayashi M. J Neurophysiol 1994;72(6):2980.
[76] Hansen CM. J Paint Technol 1967;39:104.
[77] Hansen CM. J Paint Technol 1967;39:511.
[78] van Krevelen DW. Properties of polymers: their correlation with chemical structure; their numerical estimation and prediction from group contributions. New York: Elsevier Science, 1990 (p. 536 and 575).
[79] SDK, Molecular simulations Inc., San Diego, CA.
[80] Cerius2, Version 3.0, Molecular simulations Inc., San Diego, CA.
[81] Rappe AK, Goddard III WA. J Phys Chem 1991;95:3358–63.
[82] Walker G, Lewis N, private communication.
[83] Gusev AA, Arizzi S, Suter UW. J Chem Phys 1993;99(3):2221.
[84] Gusev AA, Suter UW. J Chem Phys 1993;99:2228–34.
[85] Takeuchi H, Okazaki K. Makromol Chem Macromol Symp 1993; 65:81–8.
[86] Takeuchi H. J Chem Phys 1990;93:2062 (see also Refs. [83,84]).
[87] Crank J. The mathematics of diffusion. Oxford: Clarendon, 1989.
[88] Polymer handbook, New York: Wiley, 1989.